



# CFD Investigation of a Co-Flow Nozzle for Cold Spray Additive Manufacturing Applications

Amit Kumar Sharma<sup>1,2</sup> · Ashish Vashishtha<sup>1,2</sup> · Dean Callaghan<sup>1,2</sup> · Srinivasan Rao Bakshi<sup>3</sup> · M. Kamaraj<sup>3</sup> · Ramesh Raghavendra<sup>4</sup>

Submitted: 9 July 2023 / in revised form: 3 March 2024 / Accepted: 5 March 2024  
© The Author(s) 2024

**Abstract** This current work evaluates the efficacy of a co-flow nozzle for cold spray applications with the aim of mitigating nozzle clogging issues, which can occur during long-duration operations, by replacing the solid wall of a divergent nozzle section with an annular co-flow fluid boundary. Simulations were conducted on high-pressure nitrogen flowing through convergent–divergent (C–D) axisymmetric nozzles, with a stagnation pressure of 6 MPa and a stagnation temperature of 1273 K. In these simulations, Inconel 718 particles of varying sizes (15  $\mu\text{m}$  to 35  $\mu\text{m}$ ) were modeled using a 2-way Lagrangian

technique, and the model's accuracy was confirmed through validation against experimental results. An annular co-flow nozzle with a circular cross section and straight passage covering the primary C–D nozzle has been designed and modeled for cold spray application. Co-flow was introduced to the reduced nozzle length to compensate for particle velocity loss at higher operating conditions. It was found that co-flow facilitates momentum preservation for primary flow by providing an annular gas boundary, resulting in increased particle speed for a longer axial distance beyond the nozzle exit of the reduced divergent length nozzle. The particle acceleration performance of the reduced divergent section nozzle, when combined with co-flow, is comparable to the original length nozzle.

**Keywords** cold gas dynamic spraying · computational fluid dynamics · nozzle design · particle velocity

This article is an invited paper selected from presentations at the 2023 International Thermal Spray Conference, held May 22–25, 2023, in Québec City, Canada, and has been expanded from the original presentation. The issue was organized by Giovanni Bolelli, University of Modena and Reggio Emilia (Lead Editor); Emine Bakan, Forschungszentrum Jülich GmbH; Partha Pratim Bandyopadhyay, Indian Institute of Technology, Karaghpur; Šárka Houdková, University of West Bohemia; Yuji Ichikawa, Tohoku University; Heli Koivuluoto, Tampere University; Yuk-Chiu Lau, General Electric Power (Retired); Hua Li, Ningbo Institute of Materials Technology and Engineering, CAS; Dheepa Srinivasan, Pratt & Whitney; and Filofteia-Laura Toma, Fraunhofer Institute for Material and Beam Technology.

✉ Amit Kumar Sharma  
aksharma2124@gmail.com

- <sup>1</sup> Department of Aerospace and Mechanical Engineering, South East Technological University, Carlow, Ireland
- <sup>2</sup> The Centre of Research and Enterprise in Engineering (engCORE), South East Technological University, Carlow, Ireland
- <sup>3</sup> Department of Metallurgical and Material Engineering, Indian Institute of Technology, Chennai, India
- <sup>4</sup> SEAM Research Centre, School of Engineering, South East Technological University, Waterford, Ireland

## Introduction

Cold gas dynamic spray (cold spray) has emerged to be the most attractive non-thermal metal deposition process that has garnered significant interest from researchers and industry due to its potential in the coating, repair, and additive manufacturing fields (Ref 1). During the cold spray process, particles are accelerated at high pressure with a preheated supersonic gas stream above the critical velocity (for powder substrate combination), but below the erosion velocity, to achieve the bonding (Ref 2). Numerous sectors, including aerospace, automotive, electronics, marine, medical, oil and gas, and renewable energy, are increasingly using cold spray additive manufacturing (CSAM) to build stand-alone metal components or to repair damaged metal components (Ref 3–6). Cold spray's

flexibility of operation and high deposition rate along with the ability to deposit a diverse range of conventional materials and advanced alloys like high entropy alloys (HEA), amorphous alloys, metal matrix composites (MMC) on a wide variety of substrates gives it an edge over other metal additive manufacturing methods (Ref 7).

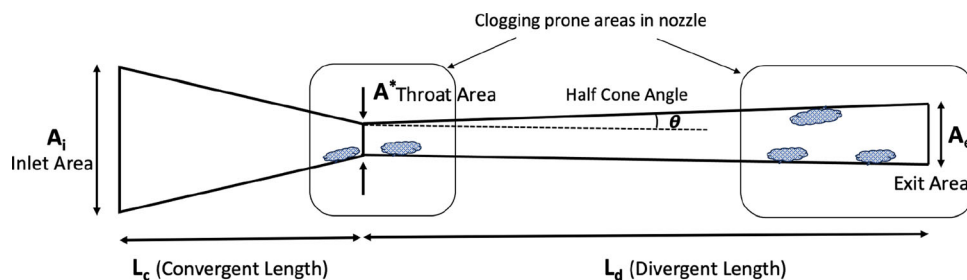
The performance of a cold spray system can be assessed by deposition quality & efficiency and metal powder acceleration. The three main parameters, that affect the performance are: input power (gas stagnation pressure and temperature at nozzle upstream), powder & substrate material properties, and nozzle efficiency. The two most utilized carrier gases are nitrogen and helium. Higher consumption of the carrier gases during operation and clogging phenomenon occurring at the throat and in the divergent section of the nozzle are the two major bottlenecks to be solved for long-duration continuous operations of a high-pressure cold spray system aiming for additive manufacturing. Clogging generally occurs when fast-moving particles bond to the nozzle's inner surface instead of continuing downstream toward the substrate. The particles gradually build up and obstruct the nozzle passage inhibiting efficient particle acceleration and leading to lower or no deposition onto the substrate. Additionally, particle layers adhered to the inside surface of the nozzle reduce the working cross-sectional area. This lowers the flow velocity and therefore lowers particle velocity, compromising the particle's capacity to reach their critical velocity at the substrate. This becomes more severe as particle velocity and temperature increases. Nozzle clogging usually occurs in two sections of a converging-diverging (CD) nozzle, first at the nozzle throat and secondly downstream of divergent length as depicted in Fig. 1. The two primary factors that contribute to nozzle clogging are the high temperature of the nozzle wall and particle dispersion as highlighted by Wang et al. (Ref 8) which is consistent with the findings by Ozdemir (Ref 9). Gas temperature, nozzle wall roughness, nozzle material, the intensity of inter-particle collision and collision with the nozzle wall, throat radius, and convergent and divergent length of the nozzle are some of the deciding factors in particle adherence to the wall. Considering all the above factors, along with sufficient particle velocity and

temperature, a conducive environment is produced leading to the particles bonding to the wall and in turn creating further buildup leading to nozzle clogging (Ref 10-13).

In general, dense, and low melting point powder materials are known for their propensity to clog which include aluminum, copper, nickel, stainless steel, Inconel, and titanium (Ref 14-18). These materials tend to deform and adhere more readily, furthermore, the low melting point makes them susceptible to premature melting or softening resulting in clogging issues during the cold spray deposition. Cold spray nozzles are often manufactured from materials such as tool steel, alloys, metal carbides, and cermets, making it uneconomical to change clogged nozzles frequently owing to the high costs of manufacturing such nozzles (Ref 19-21). Although it is possible to clean nozzles and restore them to their original specification, this necessitates monitoring the operation, stopping it when clogging occurs and the additional machining processes lead to additional cost. The preparation of a powder mixture consisting of materials prone to clogging alongside ceramic powder could indeed result in a reduction in nozzle clogging. However, this approach introduces the risk of undesired material deposited onto the substrate (Ref 22).

The cold spray system utilizes convergent-divergent (CD) nozzles with a circular cross section. These nozzles have an elongated divergent section and typically an exit diameter below 10 mm. The longer divergent section nozzle with a lesser half cone angle can provide streamlined straight flow in comparison to a shorter divergent length nozzle of the same design Mach number, but it causes significant frictional losses at the nozzle wall's boundary layer in the divergent section. The isentropic design exit Mach number of convergent-divergent nozzle depends on the area ratio at nozzle exit and throat, but not on divergent length as it does not account for frictional losses. Due to significant friction losses at the wall boundary in a longer divergent length nozzle with a smaller than 10 mm diameter passage, the exit Mach number can be significantly lower than the design Mach number as the boundary layer at the wall can influence the effective passage of supersonic flow. Also, it can have a higher exit temperature of gas than compared to the isentropic design exit temperature due to losses in the boundary layer.

**Fig. 1** Schematic illustration of CD nozzle clogging in cold spray process



A clogged region is typically found toward the downstream region of the divergent section of the nozzle. Reducing the divergent length of the nozzle without compromising the particle exit velocity could potentially eradicate the areas that were frequently prone to clogging during long continuous cold spray operations. However, reducing the divergent length has an adverse effect on the particles, by reducing their velocity at the nozzle exit as the particles have less residence time inside the nozzle to accelerate (Ref 23). Thus, it is required that if the nozzle length is to be reduced, additional measures must be taken to compensate for losses in particle velocity. Even though the supersonic nozzle is central to a cold spray system's performance, very few studies have been carried out on unconventional nozzle designs that can enhance deposition efficiency and build quality (Ref 7, 24-30). In this study, a volume of high-speed fluid encircling the primary flow is introduced as a coaxial co-flow nozzle as shown in Fig. 2 to shorten the divergent section length, and at the same time, compensating for the velocity loss sustained by the particles by providing fluid based wall rather than a solid wall.

The concept of coaxial nozzles has been explored through experimental investigations in an open jet facility, where primary supersonic flow is surrounded by sonic annular co-flow (Ref 31, 32). Additionally, Sharma et al. conducted a computational fluid dynamics study to examine the application of co-axial nozzles in cold spray processes (Ref 33, 34). It was observed that under all operating conditions, the sonic co-flow around the supersonic jet not only elongated the supersonic core by increasing the number of shock cells but also retained momentum in the jet's decay zone by inhibiting mixing with the surrounding static atmosphere. Particle acceleration may continue to increase over extended distances within the elongated supersonic core length. The higher particle acceleration after the nozzle exit can make it possible to shorten the divergent section length, which in turn can reduce the

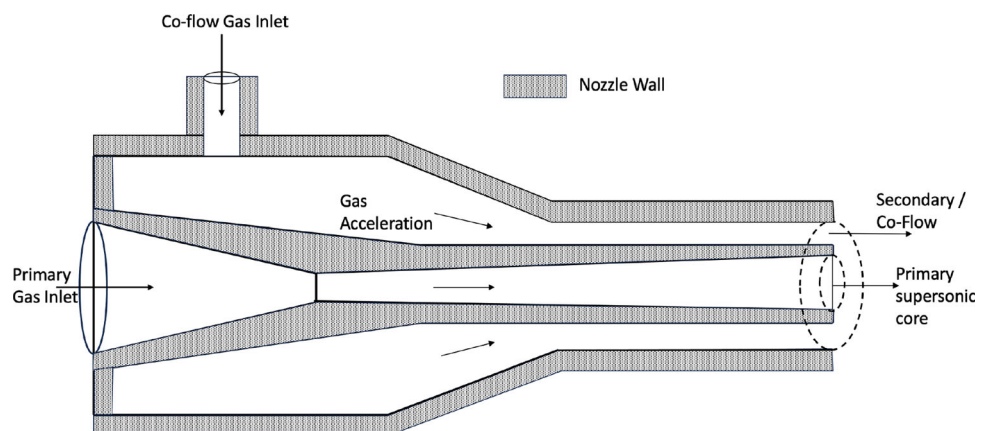
clogging phenomenon. Apart from the elongation of the nozzle's supersonic core length, the co-flow nozzle can be helpful in mitigating the acoustic signature of a supersonic jet while impacting the substrate by suppressing the Mach wave emission (Ref 35). In addition, co-flow can also have the added advantage of assisting nozzle wall cooling as lower-temperature annular co-flow gas passes over the primary flow walls during the operation. Significant advances in computational fluid dynamics (CFD) (Ref 36, 37) research of cold spray processes enable the performance of the novel nozzle to be evaluated in conjunction with experimentally obtained results.

This study primarily aims to develop an understanding on the effect of a reduced divergent length on particle acceleration in a cold spray CD nozzle by using CFD simulations. Additionally, this study investigates the mitigation strategies for any reduced performance of the CD nozzle by introducing the annular co-flow region, which provides a moving fluid boundary to preserve the momentum of gas flow exiting from the reduced divergent length nozzle. The following sections will analyze the results of the axisymmetric numerical simulations for four different divergent length nozzles by comparing gas and particle velocity for different sizes of particles, i.e., 22, 35, 15-35  $\mu\text{m}$ . In addition, a shorter nozzle using co-flow is compared with the original nozzle while maintaining all other nozzle design parameters the same, to understand the effectiveness of the co-flow.

## Design and Modeling Method

All the numerical simulations carried out in this study are performed using ANSYS Fluent 2021 R1 with gas and particle simulations carried out using a two-dimensional axisymmetric computational domain.

**Fig. 2** Representative diagram of co-flow nozzle for cold spray application



## Geometry and Computational Domain

The simulations are performed for a standard convergent-divergent nozzle along with a co-flow nozzle by integrating an annular passage as shown in Fig. 2. The original convergent-divergent nozzle has a divergent length (DL) of 189 mm. The operating conditions for primary flow that accelerate the Inconel 718 powder particles are adopted according to a high-pressure cold spray system operating at 6 MPa of stagnation pressure and 1273 K of stagnation temperature. The exit-to-throat area ratio and the convergent section were kept constant for all nozzle designs while the divergent length was varied from 15 to 42D, where D is the nozzle exit diameter. Until a specific reduction in divergent length is reached, the particle speed exhibits minimal decline or, in certain instances, remains unchanged. In our parametric investigation, we observed a small decrement (approximately 2.5%) in particle velocity with divergent length reduction up to 129 mm as shown in Fig. 3 which compares the mean particle velocity for DL 129 and DL 189 nozzle. However, noteworthy disparities emerged with a reduction from divergent length of 109 mm (DL 109) onward. Consequently, nozzles with a divergent length less than or equal to 109 mm are included in this study. The study includes simulations of three distinct divergent length nozzles DL 109, DL 99, and DL 69 in addition to the original length DL 189 nozzle. The corresponding simulation conditions of all four designs (DL 189, DL 109, DL 99 & DL 69) with varying divergent lengths along with co-flow conditions are summarized in Table 1.

As illustrated in Fig. 2, a co-flowing annular straight channel is coupled to the divergent portion of the nozzle, allowing the central jet to expand into the sonic annular flow. Figure 4 shows the computational domain and computational grid for the co-flow nozzle used in the simulations. A straight chamber is attached at the beginning of the convergent section of the nozzle to stabilize the gas flow. The computational domain comprises a stagnation

chamber, a particle discharge tube, the nozzle along with the co-flow region, and an extended expansion region. A two-dimensional axisymmetric model was utilized in the analysis with quadrilateral elements which allows a considerable reduction in computational time. The structured mesh was constructed to complement the respective flow phenomena and tested to provide a mesh-independent solution. The mesh was refined at the near-wall region to capture the boundary layer flow. The throat and exit region of the nozzle was refined adequately to visualize the flow gradient and capture the shock patterns. Special attention was given to the exit refinement to ensure that there was no change in flow patterns during the grid independence study.

## Boundary Conditions

The boundary conditions at the nozzle inlet (pressure inlet) were set to 6 MPa and 1273 K for Inconel 718 in all of the simulations, while atmospheric static pressure was set at the outlet zone. At the co-flow nozzle (pressure inlet boundary) 3 MPa and 300 K were applied to understand the influence on particle acceleration and enhancement of the primary flow core length. For both co-flow and primary inlet, nitrogen (N<sub>2</sub>) was employed as the working gas in the computational study. The stagnation chamber has negligible velocity thus the total and static temperature and pressure are equal. An extended domain was created at the exit of the nozzle to analyze the particle's velocity profile. For the simulation case without co-flow, the co-flow inlet was assigned a wall boundary condition. All boundary conditions employed in the simulation have been explicitly listed in Table 2 for reference. In the experimental work, 15–35  $\mu\text{m}$  Inconel powder particle was utilized with a mean particle size of 22  $\mu\text{m}$  with the largest being 35  $\mu\text{m}$ . Thus, for the computational analysis these three sizes, i.e., 22, 35  $\mu\text{m}$ , and a variation of 15–35  $\mu\text{m}$  were intentionally chosen and injected from the nozzle inlet at 60 g/min to encompass the range of particle sizes encountered in the actual experiments.

## Simulation Set-Up

The nozzle configurations in Table 1 were simulated with a two-dimensional axisymmetric solver. To account for compressibility effects, the ideal gas law was used for density calculations and nitrogen was used as the process gas. An implicit density-based solver was used under steady-state conditions as it responds favorably to compressible flows in the supersonic region. In highly compressible flow, the viscosity of the gas tends to change with temperature, thus the 3-coefficient Sutherland law is utilized as it is widely recommended for supersonic gas flows. The advection upstream splitting method (AUSM) scheme was employed as the flux

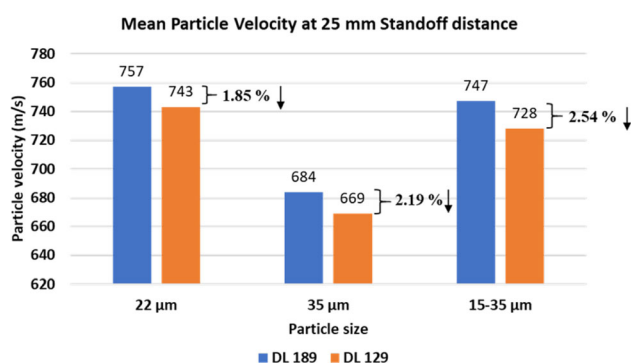


**Fig. 3** Mean particle velocity at 25 mm standoff distance for DL 189 & DL 129 for 22  $\mu\text{m}$ , 35  $\mu\text{m}$ , and 15–35  $\mu\text{m}$  particle size

**Table 1** Simulated cases (NCF- Without Co-Flow, CF- With Co-Flow, Gas: Nitrogen)

Sr. No.	Cases	Cone Half-Angle (°)	Without co-flow	With co-flow (3 MPa & 300 K)	Operating condition	Material	Particle size used in CFD study
1a	DL69	1.038	NCF	...	6 MPa & 1273 K	Inconel 718	22 μm,
1b							35 μm,
1c							(15-35 μm)
2a	DL99	0.723	NCF	With CF	6 MPa & 1273 K	Inconel 718	22 μm,
2b				2a', 2b', 2c'			35 μm,
2c							(15-35 μm)
3a	DL109	0.657	NCF	...	6 MPa & 1273 K	Inconel 718	22 μm,
3b							35 μm,
3c							(15-35 μm)
4a	DL189	0.378	NCF	...	6 MPa & 1273 K	Inconel 718	22 μm,
4b							35 μm,
4c							(15-35 μm)

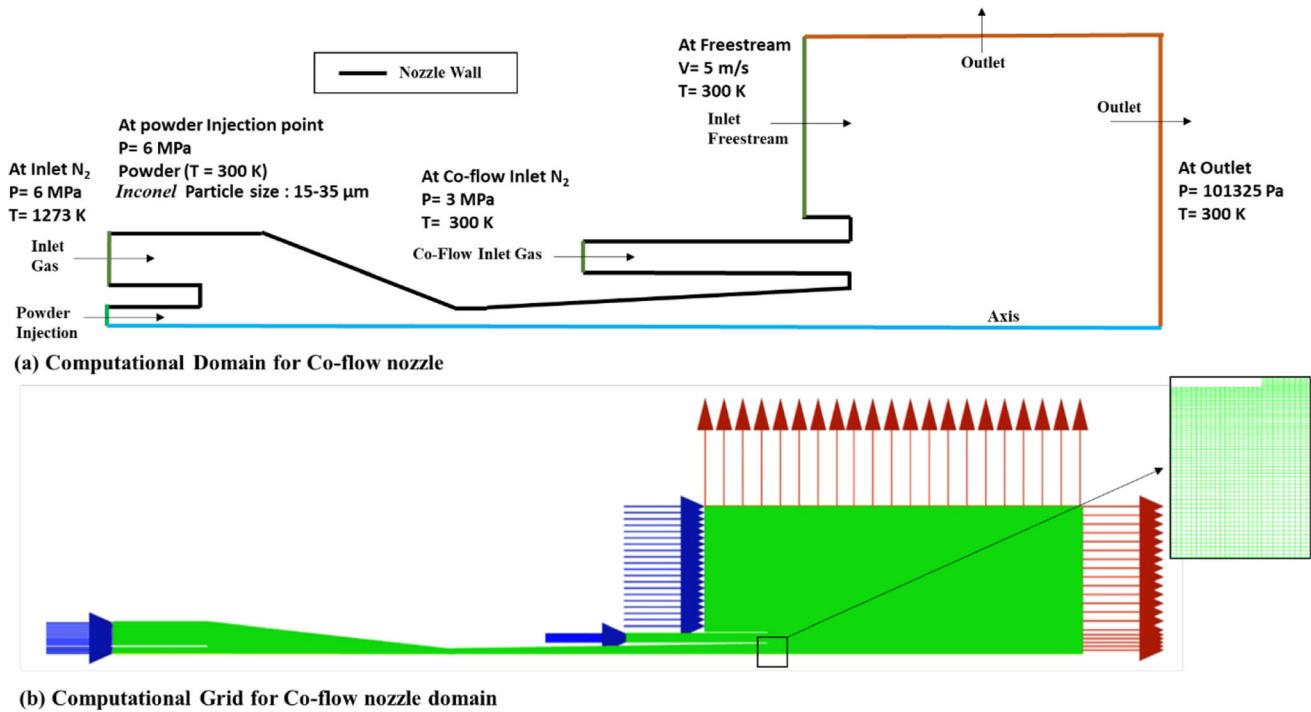


**Fig. 4** (a) Computational domain and (b) Computational grid for co-flow nozzle

**Table 2** Boundary conditions

	Name	Condition type	P	T	DPM
BC 1	Inlet	Pressure inlet	Specified	Specified	Escape
BC 2	Inlet powder inj.	Pressure inlet	Specified	Specified	Injection
BC 3	Inlet co-flow	Pressure inlet	Specified	Specified	Escape
BC 4	Inlet Free stream	Velocity inlet	Specified	Specified	Escape
BC 5	Outlet	Pressure outlet	Specified	Specified	Escape
BC 6	Wall	Adiabatic no -slip	...	...	Reflect

type along with the Green-Gauss node-based gradient method for discretization. The flow fields were solved with second-order accuracy until the necessary number of iterations reached an acceptable level of convergence. As the flow field lacks regions of flow separation or recirculation, the 2-equation standard  $k-\epsilon$  model of turbulence was found adequate for this study. High-order term relaxation (HOTR) and convergence acceleration for stretched meshes (CASM) were enabled to accelerate convergence in the density-based solver (DBS-implicit) along with solution steering (Ref 24, 25). The FMG initialization method was used to get an initial solution for the solver to initiate the simulation and reduce the computational time. Particle injection into the nozzle inlet was carried out using a discrete phase modeling algorithm. For the study of 22 and 35  $\mu\text{m}$  particle size, 100 particles were injected through surface injection, while for the simulation of particles with a size range of 15-35  $\mu\text{m}$  1000 particles were injected via group injection method and distribution according to the Rosin–Rammler approach (Ref 38). To validate the numerical model, a single simulation was conducted, simulating 5000 particles within the size range of 15-35  $\mu\text{m}$  for the DL 189 case. This simulation aimed to compare the results with experimental data. A two-way Lagrangian approach was utilized to simulate particle acceleration, as it is more effective for obtaining higher-quality results. Furthermore, the high-Mach number drag law was used to include the effect of compressibility. The stochastic-tracking type model discrete random walk (DRW) method was used to account for particle dispersion due to turbulence effects. By using this, the generation of a fluctuating velocity is realized by a Gaussian distribution function (Ref (33, 34)).

### Grid Independence and Model Validation

Three different mesh sizes of grid fine (0.075 mm), medium (0.1 mm), and coarse (0.125 mm) were used to simulate the central nozzle without co-flow. Particles were injected at the nozzle inlet and non-dimensional gas and particle velocities ( $V/V_{\text{Design}}$ ) were plotted against a non-dimensional axial location ( $X/D$ ).  $V$  represents the respective gas or particle velocity, while  $V_{\text{Design}}$  is the calculated gas velocity using isentropic relations at nozzle exit for a particular design Mach number nozzle,  $M_{\text{Design}}$ . Figure 5 depicts the non-dimensionalized gas and particle velocities obtained from simulations. These velocities are normalized using the gas speed generated by a nozzle operating with nitrogen at a stagnation temperature of 1273 K, using isentropic relations as explained by Eq 1, 2, and 3. The comparison of gas phase velocities at different grid resolutions reveals that there is negligible variation in the nozzle exit velocity and the post-nozzle fluctuations, which corresponds to shock cell formations in the flow field. The

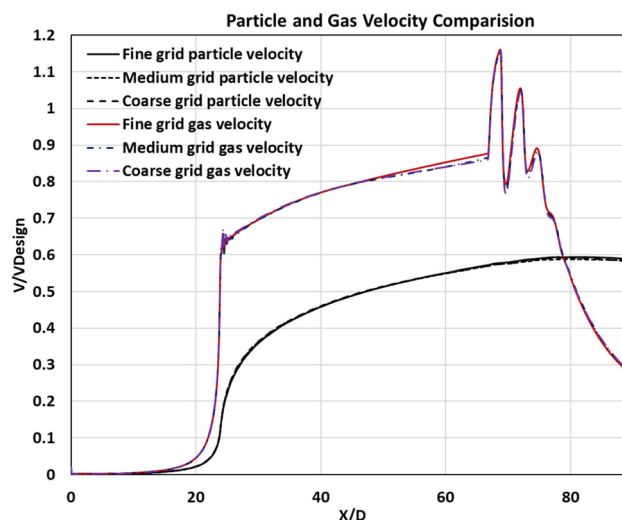


Fig. 5 Grid independence test for different grid sizes

particle acceleration results obtained from the three grid resolutions are also compared. Notably, there are no substantial deviations in particle acceleration among the different grids, leading to the selection of the medium grid resolution for further simulation to reduce computation time.

$$V_{\text{Design}} = M_{\text{Design}} * \sqrt{\frac{\gamma * R U * T_e}{M W_{\text{gas}}}} \tag{Eq 1}$$

$$\frac{T_e}{T_o} = \left[ 1 + \frac{\gamma - 1}{2} M_{\text{Design}}^2 \right]^{-1} \tag{Eq 2}$$

$$\frac{A_e}{A^*} = \frac{1}{M_{\text{Design}}} \left[ \left( \frac{2}{\gamma + 1} \right) \left( 1 + \frac{\gamma - 1}{2} M_{\text{Design}}^2 \right) \right]^{\frac{\gamma + 1}{2(\gamma - 1)}} \tag{Eq 3}$$

The experiment was conducted using a commercially available Plasma Giken cold spray system with the original nozzle of the divergent length of 189 mm (DL 189), operating at a stagnation temperature of 1273 K and stagnation pressure of 6 MPa with the injection of Inconel 718 powder with a size range of 15-35  $\mu\text{m}$ . The particle velocity at a 25 mm standoff distance was obtained using a HiWatch CS2 particle velocity probe. Numerical simulations were then carried out with the experimental condition and particle velocity distribution result at 25 mm standoff distance was obtained and plotted along with experimental mean velocity as shown in Fig. 6. In numerical simulation, the mean velocity line represents the mean velocity of 5000 particles injected into the particle pipe in the simulation, while the neutral axis represents the centerline of the nozzle. It can be seen that the simulation results are well matched to the experimental results where simulated mean particle speeds were found to be within 4% of the mean velocity obtained from the particle velocity probe as

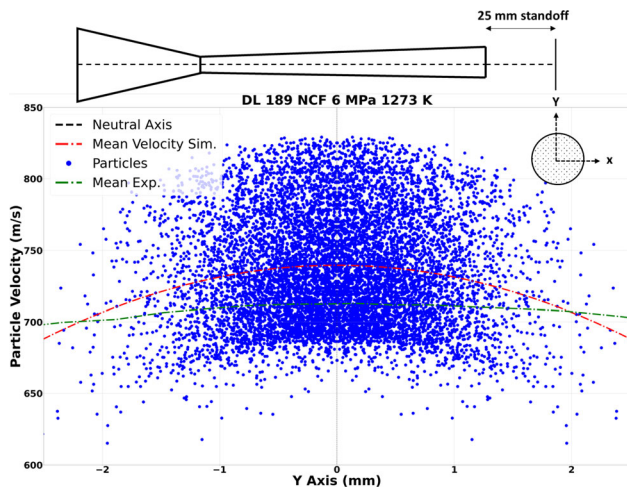


**Fig. 6** Particle velocity distribution for DL 189 at 6 MPa 1273 K for 15–35  $\mu\text{m}$  particle size at 25 mm standoff distance

represented in Fig. 6 (private communication IIT Madras) (Ref 39). Additionally, the upper and lower limits of particle velocities from the simulation fell comfortably within the experimental range, thereby confirming the validation of the numerical model for the current nozzle design study.

## Results and Discussion

### Effect of Reduction in the Divergent Length

In this section, comprehensive numerical simulations were performed for each of the four cases as outlined in Table 1. Different divergent lengths of 69, 99, 109, and 189 mm are considered, represented by DL 69, DL 99, DL 109, and DL 189, respectively, under no co-flow conditions (NCF) at a stagnation pressure of 6 MPa and the stagnation temperature of 1273 K. The investigation was systematically carried out across three distinct sets, with the first set dedicated to simulating all cases (1a, 2a, 3a, and 4a) for a particle size of 22  $\mu\text{m}$ . The second set delved into simulations tailored for a particle size of 35  $\mu\text{m}$  (1b, 2b, 3b, and 4b), while the third set encompassed a thorough exploration of the entire powder particle size range (15–35  $\mu\text{m}$ ) across all divergent length, i.e., (case 1c, 2c, 3c and 4c). Within each set, the centerline gas speed, mean particle velocities and velocity contours are analyzed for different divergent length nozzles while keeping the exit Mach number the same and varying cone half-angle between 0.378 and 1.038<sup>0</sup>. This parametric approach aims to provide a detailed understanding of how varying divergent lengths impact performance, contributing valuable insights to the broader understanding of the subject.

### 22 $\mu\text{m}$ Particle Size

Figures 7 and 8 depict the gas phase velocity variation and contours for DL 69, 99, 109 & 189 cases at 6 MPa 1273 K Inconel for 22  $\mu\text{m}$  particle size. The gas velocity profiles follow the same trend in the convergent section of the nozzle and the supersonic jet profile, the number of shock cells after the nozzle exit is also the same, with a marginal reduction in shock strength and elongation in axial core length. To facilitate reader comprehension, we have incorporated graphical annotations, highlighting key parameters such as nozzle exit, core length, and shock cell for the DL 189 case under no co-flow conditions (NCF). These marked terms serve as interpretive cues, aiding in the understanding of analogous parameters in the context of the other cases. As the length of the nozzle becomes shorter the increase in gas exit velocities is due to a reduced boundary layer effect on centerline flow and reduced friction losses overall (Ref 40, 41). The expression “ $V/V_{\text{Design}}$ ” denotes the ratio of the attained gas velocity at any particular location within and outside the nozzle to the isentropic gas velocity at the nozzle exit for which the nozzle was originally designed, corresponding to a specific Mach number. It was found that the DL 69 achieved the highest gas velocity of 91.8% at the exit of the nozzle as compared to the designed mach number, while DL 99, DL 109, and DL 189 achieved 91.04, 89.94, and 85.01%, respectively. Figure 9(a) illustrates the mean particle velocity of 100 particles with a diameter of 22  $\mu\text{m}$ , which were introduced through a powder feeder tube at the centerline of the convergent section during numerical simulations. Additionally, the figure includes a zoomed-in normalized particle velocity representation Fig. 9(b) for all four cases. When the divergent length is reduced, the gas phase velocity at the centerline is seen to increase. The increase in gas velocity could directly relate to an increase in particle velocity. However, at the same time, particles get less residence time in the shorter divergent section. Thus, the combined effect leads to an overall reduction in the particle velocity as seen in the particle velocity results, thereby inferring that the reduced residence time is a dominant factor over the increased gas velocity when it comes to the shortening of the divergent section. DL 189 case showed the highest particle velocity which indicates that the longer nozzles allow for a higher residence time for particles to remain in high-speed flow, which imparts higher speed. Figure 10 illustrates the mean particle velocity trend for various nozzles at exit and a standoff distance of 25 mm. The particle velocity at the nozzle exit reduces from 740 m/s in DL 189 to 691 m/s, 672 m/s, and 624 m/s in DL 109, DL 99, and DL 69, respectively. The particle velocity exhibits an approximate 15.6% drop between DL 189 and DL 69, while DL 99 and DL 109

**Fig. 7** Axial gas velocity of DL 69, 99, 109 & 189 at 6 MPa 1273 K Inconel for 22  $\mu\text{m}$  particle size

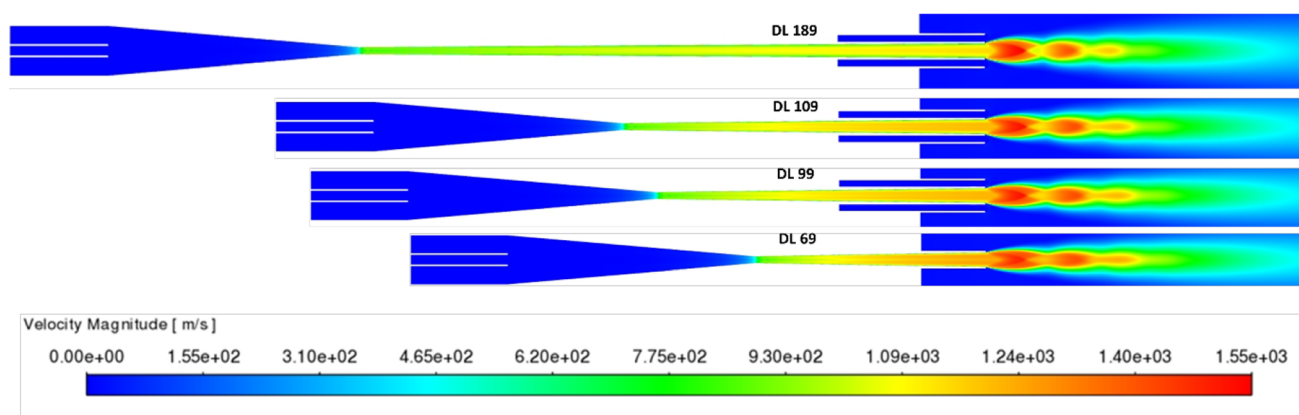
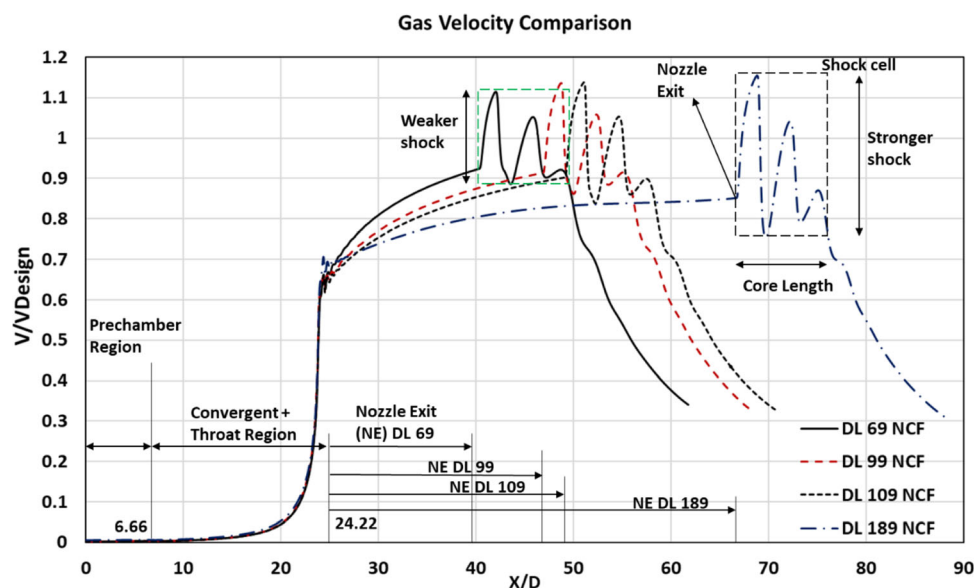


**Fig. 8** Gas velocity contours for DL 69, 99, 109 & 189 at 6 MPa 1273 K

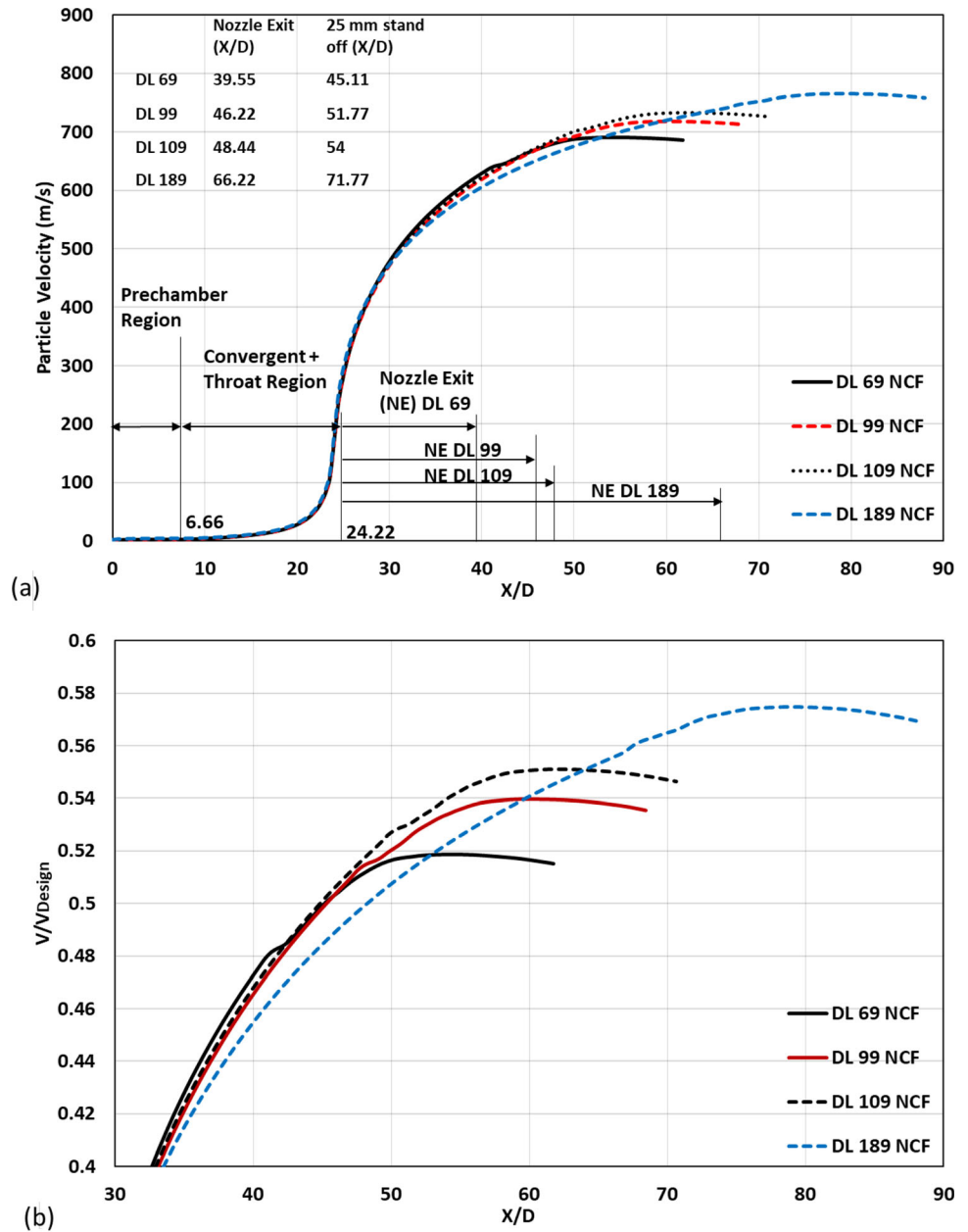
sustained a drop of 9.12% and 6.58%, respectively. Analyzing the particle velocity at a standoff distance of 25 mm from the exit, the DL 69 case experiences a 12.15% reduction, while DL 109 and DL 99 exhibit drops of 6.47% and 7.26%, respectively, in comparison to the DL 189 case. Comparing the increase in particle velocity at the standoff distance with the nozzle exit for each case, the DL 69 case demonstrates the most significant increase, approximately 41 m/s, whereas the DL 189 case has the least increment, with just 17 m/s. This trend is attributed to the higher exit gas velocity and relatively weaker shock strength in the DL 69 case compared to the DL 189 case which helps the particle accelerate more than that of larger length nozzles.

In cold spray, when particles impact the substrate, a minimum velocity (the critical velocity) is needed for the particles to bond effectively. The critical velocity mainly depends on the intrinsic properties of particles, substrate,

and process parameters (Ref 42, 43). One of the most dominant factors affecting critical velocity is the particle size. The determination of critical velocity is conducted through a semi-empirical method, wherein the velocity distribution is measured in conjunction with the deposition efficiency and particle size distribution. This process involves calculating the size and velocity of the largest particle capable of bonding to the substrate (Ref 44). Particles of larger diameter tend to be the slowest, the velocity associated with this largest and slowest bonded particle is then considered as the experimentally determined critical velocity. Thus, these large diameter particles dictate the optimum parameters of gas temperature and pressure for the process. Therefore, additional simulations were carried out for all the cases using a 35- $\mu\text{m}$  particle size to observe the effect it has on the particle velocities.



**Fig. 9** Mean particle velocity (a), zoomed-in normalized particle velocity (b) of DL 69, 99, 109 & 189 at 6 MPa 1273 K Inconel for 22  $\mu\text{m}$  particle size

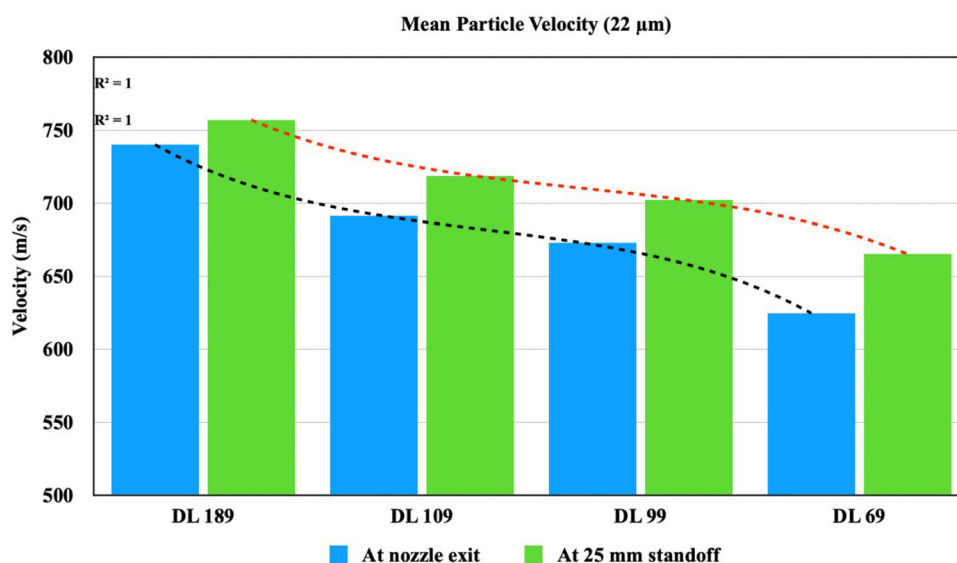


### 35 $\mu\text{m}$ Particle Size

The gas velocity profile remains consistent across varying particle sizes, exhibiting the same behavior as previously mentioned, with the highest velocity observed for the DL 69 nozzle and the lowest for the DL 189 nozzle. Figure 11(a) depicts the mean particle velocity plot of 100 Inconel particles with a diameter of 35  $\mu\text{m}$ , along with a zoomed-in normalized particle velocity representation Fig. 11(b) for all four cases DL 69, 99, 109 & 189 at 6 MPa 1273 K. Figure 12 outlines the mean particle velocity at both the nozzle exit and a 25-mm standoff distance for particles with a size of 35  $\mu\text{m}$ . Upon analyzing the mean

particle velocities at the nozzle exit, it is observed that the 35  $\mu\text{m}$  particles achieved speeds of 670.4 m/s in DL 189, 623.6 m/s in DL 109, 631.5 m/s in DL 99, and 585 m/s in DL 69 case. This indicates a 12.71% decrease in particle velocity for DL 69 compared to the DL 189 case, while DL 99 and DL 109 exhibited reductions of 5.8% and 7%, respectively. Likewise, when examining particle velocity at a standoff distance of 25 mm from the exit, DL 69 exhibited a 9.06% decrease, while DL 99 and DL 109 experienced reductions of 3.8% and 5.4%, respectively, compared to the DL 189 case. It was noteworthy to observe DL 99 outperforming DL 109 in this particular instance, as DL 109 experienced a 7% decrease, slightly more than DL

**Fig. 10** Mean particle velocity at nozzle exit and at 25 mm standoff distance for 22  $\mu\text{m}$  particle size



99 at nozzle exit. Contrary to expectations based on the divergent length and residence time concept, DL 109 should have exhibited higher particle velocity. However, unexpectedly, there was a 1.2% excess reduction in comparison to DL 99 at the nozzle exit and 1.6 % at a standoff distance, potentially attributable to numerical uncertainties or reasons unknown to the author at this juncture. From Fig. 12, it can also be observed from the trendline that particles accelerate much more effectively over a standoff distance of 25 mm when the nozzle divergent length is reduced, mirroring what was observed for the 22  $\mu\text{m}$  case. Between the standoff distance and the nozzle exit, the mean particle velocity increased by 37 m/s for DL 69, with the lowest increase in 14 m/s observed in the DL 189 case.

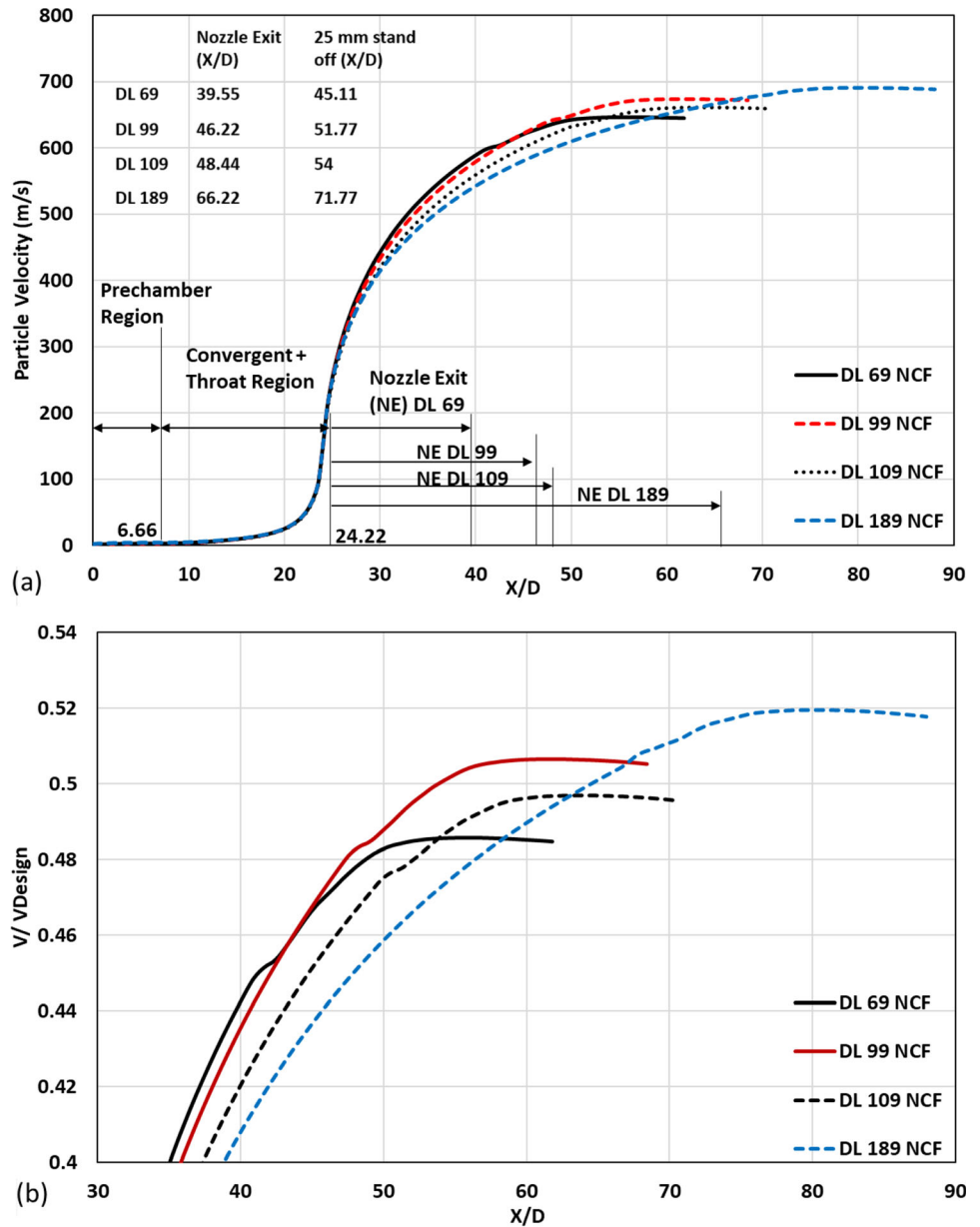
### 15-35 $\mu\text{m}$ Particle Size

When a nozzle is designed for a cold spray system the nozzle must accommodate different particle sizes across a range of pressure and temperatures. Thus, it is required to validate the reduced divergent length nozzle's performance for a range of particle sizes. Hence, particle distribution of 15-35  $\mu\text{m}$  is simulated and analyzed at the same working pressure and temperature conditions of 6 MPa & 1273 K and results can be seen in Figs. 13 and 14. The trends in gas and particle velocity closely mirror those observed for particle sizes of 22  $\mu\text{m}$  and 35  $\mu\text{m}$ . Examining the mean particle velocity of 1000 particles at the nozzle exit, DL 69, DL 99, and DL 109 experienced velocity reductions of 11.4%, 4.9%, and 4%, respectively. DL 99 and DL 109 demonstrated comparable performance, with their particle velocity at the standoff distance decreasing by 3% and 2.5% compared to DL 189 while for the DL 69 case, the velocity decreased by 7.77%. Observing the increase in

individual nozzle's particle velocities across the standoff distance, DL 69 exhibited the most significant increment with 42 m/s, surpassing the DL 189 case which had the lowest increment observed. Meanwhile, DL 99 and DL 109 showed similar increments of 30 and 27 m/s, respectively.

In summary, evaluating the mean particle velocity outcomes for particle sizes of 22, 35, and 15-35  $\mu\text{m}$  allows us to assess the performance of each nozzle case (DL 69, DL 99, DL 109) against DL 189. This assessment is based on three key factors. First, the reduction in particle velocities compared to the original DL 189 nozzle, and second the increase in particle velocities over a standoff distance. The third and most crucial consideration is, how the reduction in nozzle length impacts particle velocity and whether this decrease can be compensated by implementing additional measures to maintain performance similar to that of the original length nozzle. DL 69 suffered the largest average decrement in particle velocity at nozzle exit across all three particle sizes, which is 13.23%, while at standoff, it was 9.66 % as seen in Table 3. DL 99 and DL 109 demonstrated a very close performance, exhibiting a particle velocity decrement within 1% for the particle size range of 15-35  $\mu\text{m}$ , with a maximum difference of 2.6% observed across all particle size simulations. Analyzing particle velocity gain in each individual nozzle at standoff distance spanning over all particle sizes the performance was in the order DL 69 > DL99 > DL109 > DL 189. Particle velocity gain after nozzle exit decreased as the nozzle length increased. When we are looking into different strategies to be effective in compensating the particle velocity in the shorter divergent nozzle to that of the original length the difference in particle velocity should be in an achievable range. The selection of the optimal nozzle length among the three cases (DL 69, DL 99, and DL 109)

**Fig. 11** Mean particle velocity (a), zoomed-in normalized particle velocity (b) of DL 69, 99, 109 & 189 at 6 MPa 1273 K Inconel for 35  $\mu\text{m}$  particle size



involves a tradeoff among the aforementioned factors. In the case of DL 69, the disparity in particle velocity is too substantial to be compensated for by flow control methods, such as introducing co-flow around the primary supersonic core, making its elimination necessary. Both DL 99 and DL 109 exhibit similar performance and fall within the range where particle velocity can be compensated to match that of DL 189. As the current study aims to explore how a reduced divergent length nozzle, combined with co-flow, affects performance to match that of the original nozzle, thus, a shorter nozzle DL 99 was selected for further investigation. Thus, DL 99 nozzle was adopted and its simulation with co-flow and without co-flow condition

across all three particle sizes, i.e., 22, 35, and 15-35  $\mu\text{m}$  was done and finally compared to DL 189 case.

### The Effect of Co-Flow on Reduced Divergent Length Nozzle

Considering the above discussion about the performance of nozzles at high pressure for different particle sizes, it was conceived that the DL 99 case offers the shortest divergent length nozzle without sustaining very high losses in particle velocity. At 6 MPa and 1273 K the particle velocity drop at the nozzle exit was nearly 5% for DL 99 for powder particle size range of 15-35  $\mu\text{m}$ . To compensate for this

**Fig. 12** Mean particle velocity at nozzle exit and at 25 mm standoff distance for 35 μm particle size

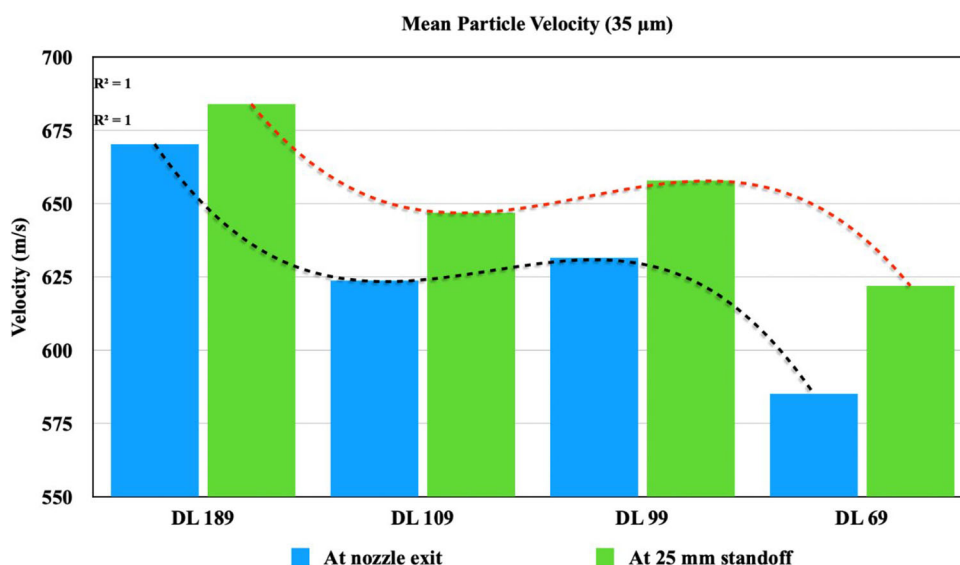
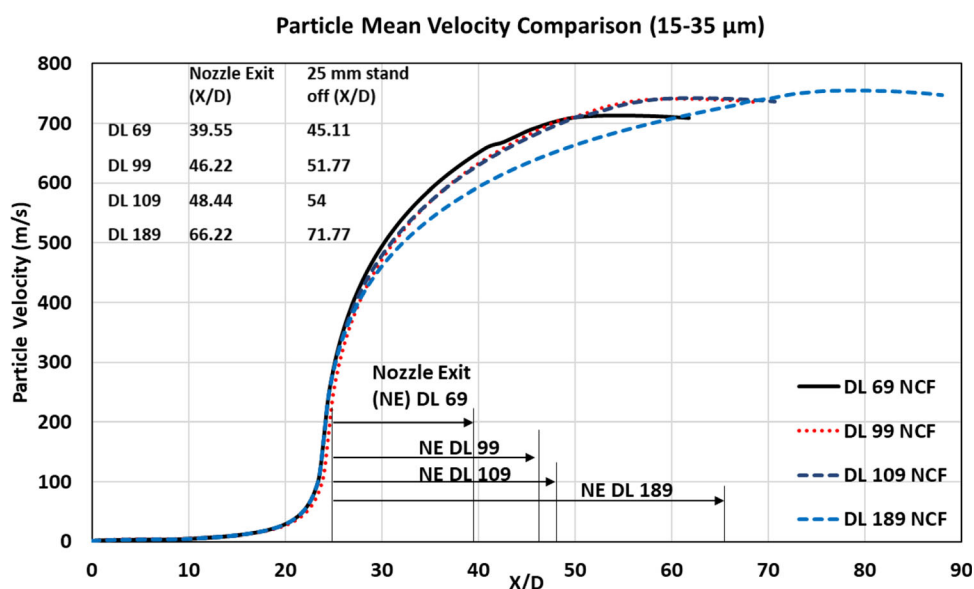


**Fig. 13** Particle velocity of DL 69, 99, 109 & 189 at 6 MPa & 1273 K Inconel for 15-35 μm particle size



loss the addition of co-flow was introduced to the nozzle. The annular co-flow around the primary supersonic core flow provides additional moving fluid boundary in place of the solid wall boundary and increases the supersonic core length of jet by inhibiting mixing with the outer atmosphere (Ref 31, 32). The numerical simulations are performed for the co-flow inlet at a pressure of 3 MPa & temperature of 300 K.

Figure 15 represents the mean axial particle velocity comparison between DL 99 CF & DL 189 NCF case (2a', 2b', 4a, and 4b) for 22 and 35 μm particles. At a standoff distance of 25 mm, for the particle size of 35 μm DL 99 CF achieved a particle velocity of 660 m/s compared to 684 m/s of DL 189. Similarly, for the 22 μm particle size, DL 99 CF reached a velocity of 743 m/s compared to

757 m/s of DL 189. In the co-flow case mean particle velocity matches with the original nozzle at 40 mm standoff distance and then continues to accelerate up to 60 mm standoff distance for 22 μm particle as seen in Fig. 16. For the 35 μm particle size, the co-flow case accelerates slowly and matches the DL 189 at 60 mm, which is true in conjunction with the fact that larger particle attains less velocity in cold spray deposition process (Ref 45). Further simulations were carried out for the DL 99 NCF, DL 99 CF, and the DL 189 NCF (2c, 2c', and 4c) conditions with a particle size distribution of between 15 and 35 μm and mean particle velocity was compared as depicted in Fig. 17(a). Figure 17(b) illustrates comparisons of gas velocity profiles for DL 99 CF and NCF conditions. Additionally, Fig. 18 displays their gas velocity magnitude

**Fig. 14** Mean particle velocity at nozzle exit and at 25 mm standoff distance for 15- 35 μm particle size

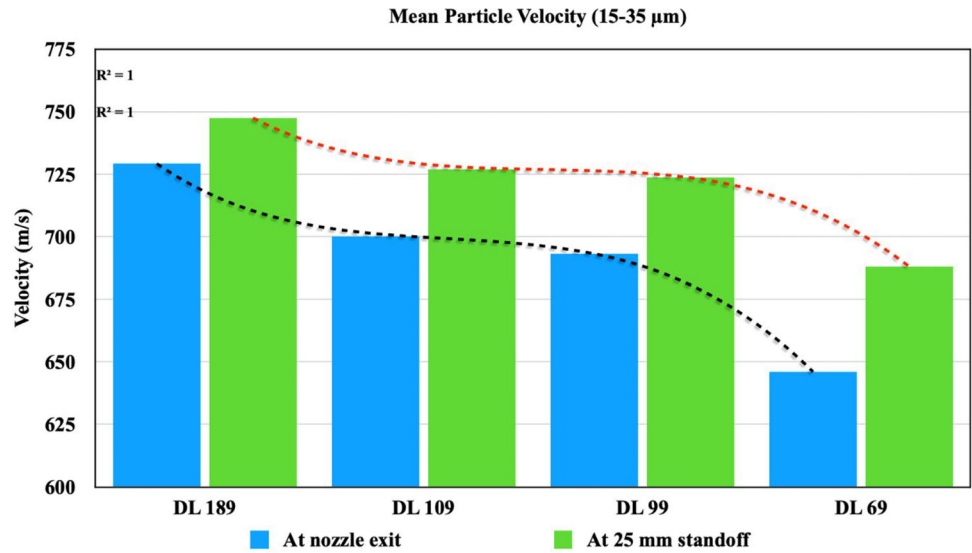


**Table 3** Mean Particle velocity decrement in DL 69, DL 99 and DL 109 at nozzle exit and standoff distance compared to DL 189 at 6 MPa 1273 K

Case	NE = at Nozzle Exit, SOD = at 25 mm standoff distance	Reduction in particle velocity compared to DL 189			Average decrement case in %
		22 μm	35 μm	15-35 μm	
DL 69	NE	15.6	12.71	11.4	13.24
	SOD	12.15	9.06	7.77	9.66
DL 99	NE	9.12	5.8	4.9	6.61
	SOD	7.26	3.8	3	4.69
DL 109	NE	6.58	7	4	5.86
	SOD	6.47	5.4	2.5	4.79

contours under the same conditions. The supersonic core length can be defined as the point of the last shock cell from the nozzle exit. The supersonic jet exiting from both the nozzle operations are under-expanded in nature. In under-expanded supersonic jet, there is expansion fan formation at the nozzle lip, which leads to an increase in centerline jet velocity in the first shock cell. The increase in centerline velocity corresponds to the expansion level (extension of first shock cell in the lateral direction). These expansion fans get reflected from the flow boundary as a shock-wave (compression wave), resulting in the decrease of flow velocity downstream of the jet in centerline. The shock waves generated will further reflect from the jet boundary as expansion waves, leading to a subsequent increase in the centerline flow velocity as we move further downstream. The oscillations in centerline velocities, as illustrated in Fig. 17(b), persist, and extend along the supersonic core length of the jet due to a sequence of expansion and compression waves (Ref 32). The

downstream of the supersonic core, the centerline jet becomes subsonic, and more mass is entrained from surroundings leading to the jet-decay region until the centerline flow becomes static. In the presence of co-flow, the expansion of the jet in the first shock cell is restricted due to the presence of a moving boundary, leading to a lower increase in centerline velocity as seen in Figs. 17(b) & 18. The co-flow presence restricts the entrainment of mass from the surrounding static atmosphere toward the centerline of the jet. This restriction results in a higher number of oscillations in centerline velocity compared to the no co-flow conditions, ultimately leading to an extended supersonic core length. The co-flow nozzle has been found to preserve the momentum of gas in the central jet flow by reducing the mixing of the supersonic core with the surrounding (Ref 46), thereby resulting in a prolonged velocity decay.

Further analyzing, Fig. 17(b) it can be seen that the core length in DL 99 CF is longer with respect to DL 99 NCF.

**Fig. 15** Axial particle velocity comparison between DL 99 CF & DL 189 for 22 and 35  $\mu\text{m}$  particle

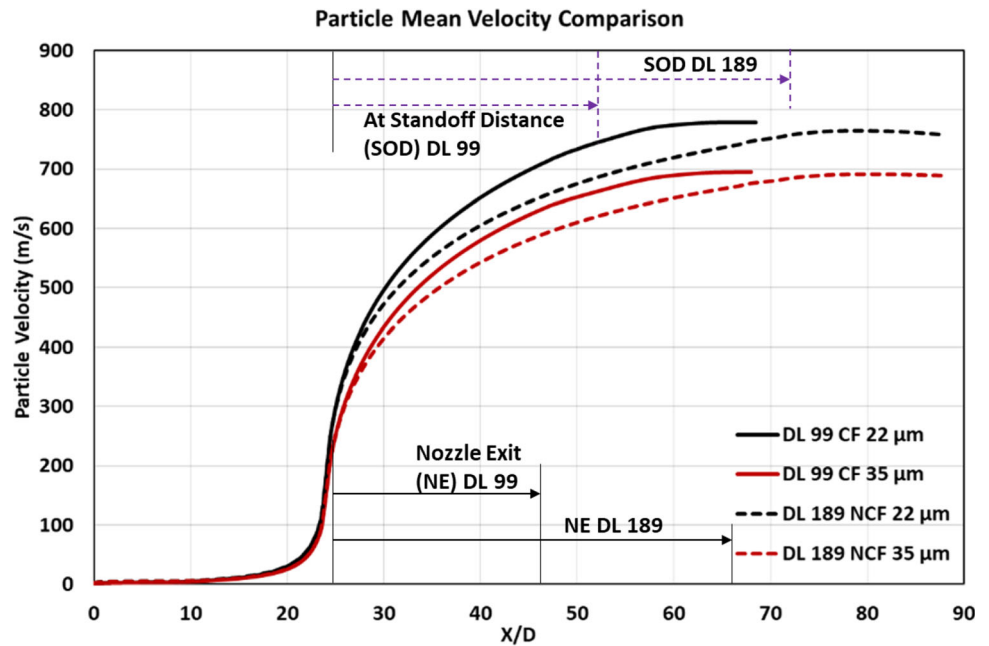
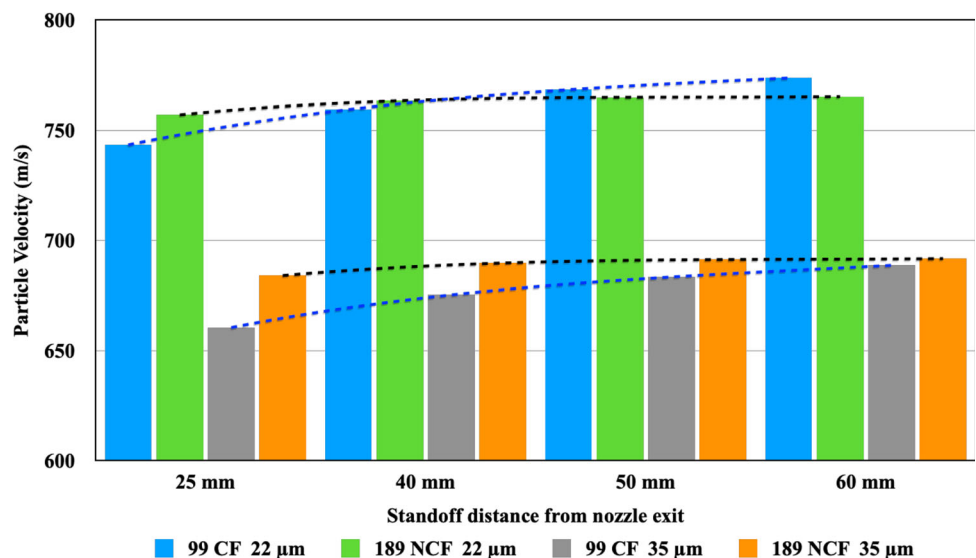


**Fig. 16** Mean particle velocity at different standoff distance for 22 and 35  $\mu\text{m}$  particle size



The same can be inferred from the gas velocity contour in Fig. 18 where the co-flow jet extends more into the downstream direction when compared to the jet of NCF condition. This extended supersonic core length, facilitated by co-flow (accompanied by a reduced nozzle length) provides the powder particle with equivalent or higher residence time to maintain high speed without the presence of a solid wall for a longer length.

Figure 19 compares the mean particle velocities at different standoff distances from the nozzle exit for DL 99CF and DL 189 NCF cases for particle sizes 15–35  $\mu\text{m}$ . The particles in the DL 99 CF case continue to accelerate after

the nozzle exit for a greater standoff distance and ultimately reach a mean velocity similar to that of the original DL 189 nozzle, with a difference of just 2 m/s at a standoff distance of 60 mm. It opens up the possibility of having an effective deposition with co-flow-assisted cold spray over an extended standoff distance of up to 60 mm. Figure 20 illustrates the distribution of particle velocities for both DL 99 CF and DL 189, considering particle sizes ranging from 15 to 35  $\mu\text{m}$  obtained from simulation results. Figure 21 represents the indicative particle position obtained from CFD simulation for DL99 CF and DL 189 at a standoff distance of 50 and 25 mm, respectively, from the nozzle

**Fig. 17** Mean particle velocity (a), gas velocity (b) comparison between DL 99 NCF and DL99 CF

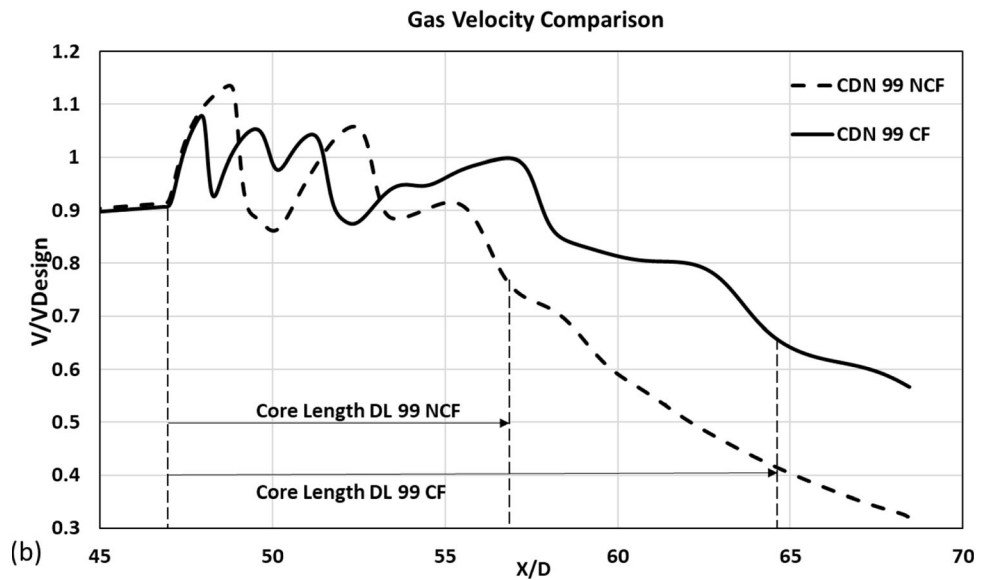
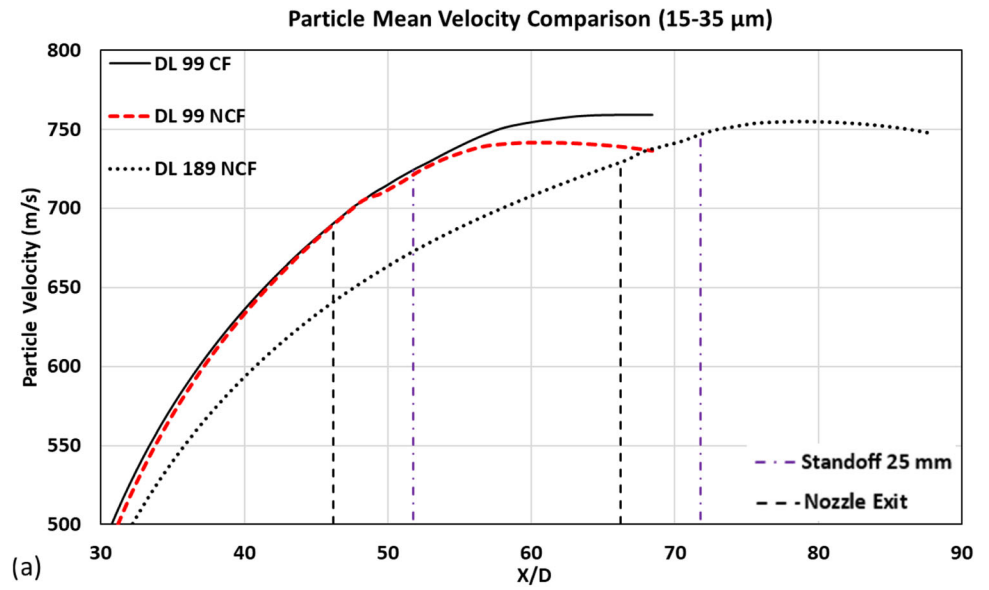


**Fig. 18** Gas velocity comparison between DL 99 NCF and DL99 CF

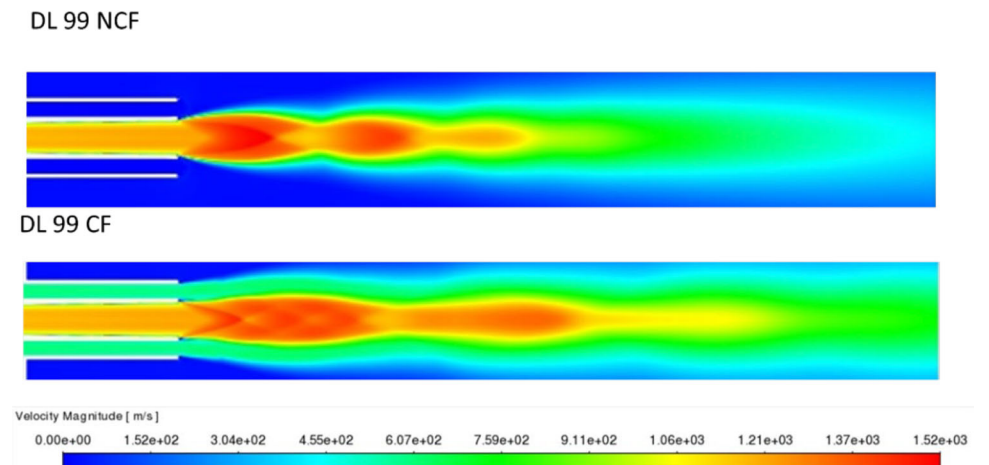


**Fig. 19** Mean particle velocity at different standoff distance for 15-35  $\mu\text{m}$  particle size

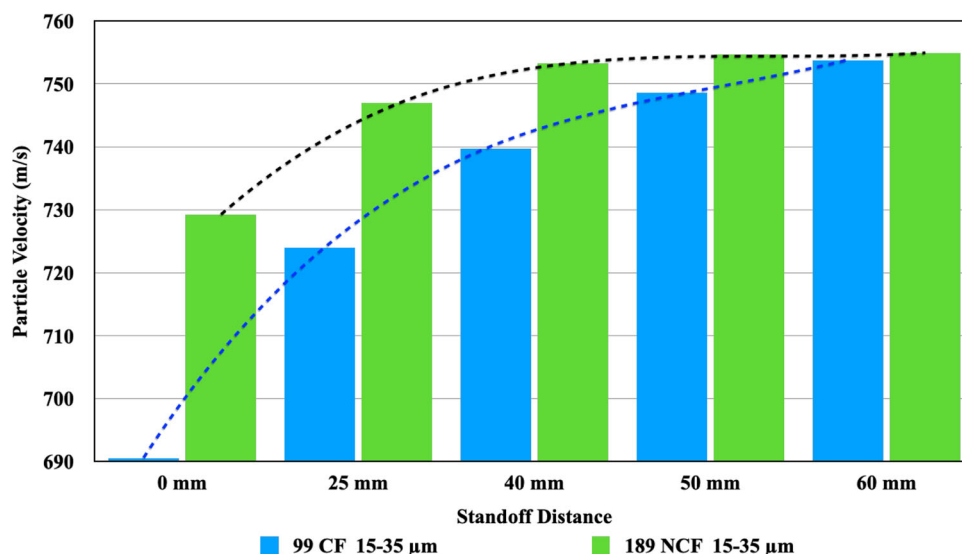
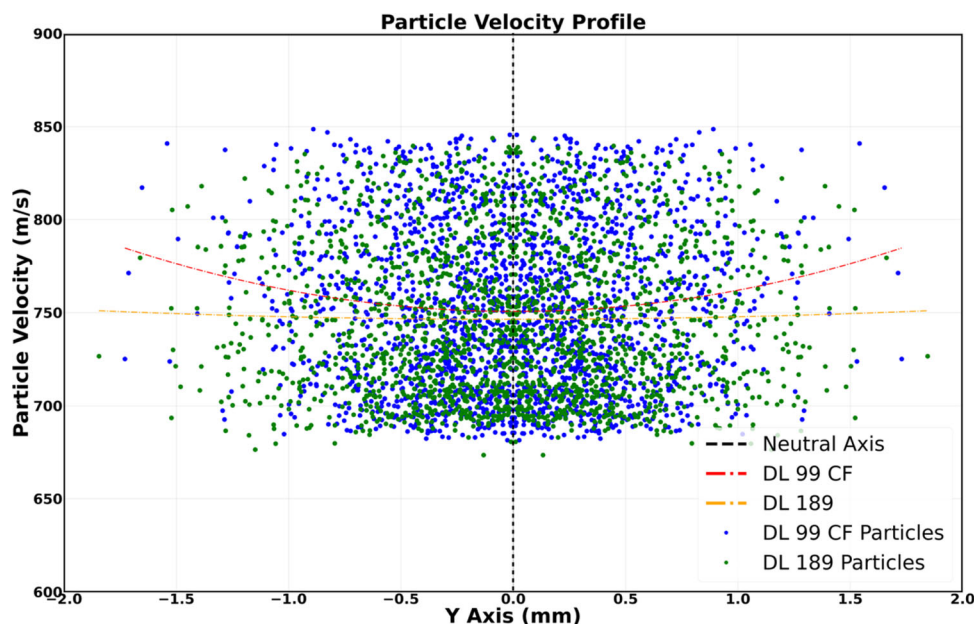


**Fig. 20** Particle velocity distribution for DL99 CF at 50 mm and DL 189 at 25 mm standoff distance from the nozzle exit with lateral axis



exit. Upon examining the velocity distribution in Fig. 20 and the particle positions in Fig. 21, it is evident that the mean value and particle dispersion are highly comparable for DL 99 CF at a standoff distance of 50 mm in comparison to DL 189 at a standoff distance of 25 mm. Consequently, it can be asserted that DL 99 with co-flow emerges as an optimal choice, demonstrating improved performance over DL 189. This is evident through its enhanced deposition capability over a larger distance, similar mean velocity, and reduced susceptibility to frictional losses and clogging.

### Conclusion

In this study, the effect of a reduction in the divergent section of a cold spray nozzle on particle acceleration is investigated by numerical simulation, operating at a stagnation pressure of 6 MPa and stagnation temperature of 1273 K with nitrogen carrier gas for 15-35  $\mu\text{m}$  Inconel 718 particles. The marginal reduction in nozzle performance, while reducing the divergent section length has been compensated by the introduction of co-flow of Nitrogen



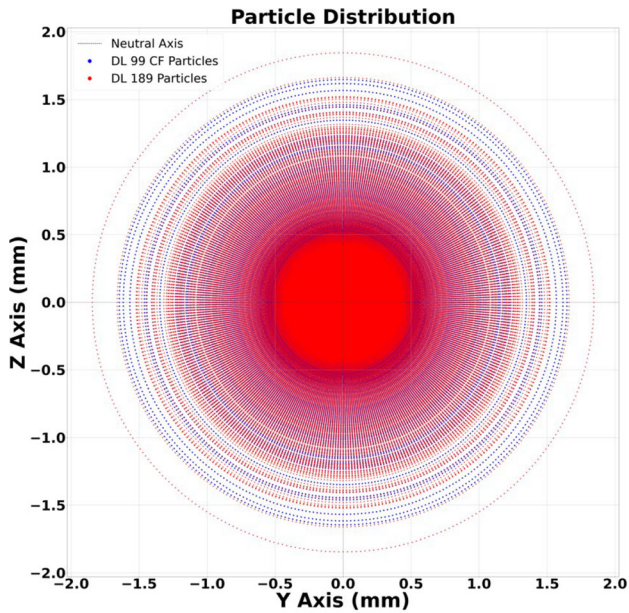


**Fig. 21** Indicative particle position for DL99 CF at 50 mm and DL 189 at 25 mm standoff distance from the nozzle exit

(same carrier gas) at 3 MPa and 300 K. The key findings to date are:

1. Reducing the divergent section length increases the exit gas velocity from the nozzle while also reducing the residence time for particles in a high-speed stream, and thus the particle's maximum attainable velocity. However, up to a certain reduced divergent length there is reduced variation in the particle velocity compared to the original nozzle.
2. Based on supersonic core-length elongation, the DL 99 CF nozzle has comparable performance with the DL 189 NCF nozzle for gas velocity and particle acceleration. The introduction of an outer co-flow in the reduced divergent section nozzle improves the performance at all lengths for supersonic core elongation as well as enhancing particle acceleration.
3. It is expected that the reduced divergent length will facilitate the reduction of clogging and lead to enhanced continuous operational time of cold spray equipment. This will be explored further in a follow-up study of this current research.

The future studies can consider introducing air in the co-flow region to reduce the cost of operation, while primary gas can be nitrogen or helium. Conducting additional numerical simulations involving a flat substrate at different standoff distances, along with experimentation and flow

visualization using a Schlieren system can provide a more comprehensive understanding of the co-flow effects. Furthermore, the integration of the co-flow method into existing industrial cold spray systems presents significant challenges, primarily stemming from design constraints and the presence of cooling jackets over the nozzles. Addressing these challenges and actively working on finding effective solutions could also be a promising avenue for future research.

**Funding** Open Access funding provided by the IReL Consortium.

**Open Access** This article is licensed under a Creative Commons Attribution 4.0 International License, which permits use, sharing, adaptation, distribution and reproduction in any medium or format, as long as you give appropriate credit to the original author(s) and the source, provide a link to the Creative Commons licence, and indicate if changes were made. The images or other third party material in this article are included in the article's Creative Commons licence, unless indicated otherwise in a credit line to the material. If material is not included in the article's Creative Commons licence and your intended use is not permitted by statutory regulation or exceeds the permitted use, you will need to obtain permission directly from the copyright holder. To view a copy of this licence, visit <http://creativecommons.org/licenses/by/4.0/>.

## References

1. R.N. Raelison, Ch. Verdy, and H. Liao, Cold Gas Dynamic Spray Additive Manufacturing Today: Deposit Possibilities, Technological Solutions And Viable Applications, *Mater. Des.*, 2017, **133**, p 266-287.
2. M. Kamaraj and V.M. Radhakrishnan, Cold Spray Coating Diagram: Bonding Properties and Construction Methodology, *J. Therm. Spray Technol.*, 2019, **28**, p 756-768.
3. S. Yin, P. Cavaliere, B. Aldwell, R. Jenkins, H. Liao, W. Li, and R. Lupoi, Cold Spray Additive Manufacturing and Repair: Fundamentals and Applications, *Addit. Manuf.*, 2018, **21**, p 628-650. <https://doi.org/10.1016/j.addma.2018.04.017>
4. W.Y. Li, K. Yang, S. Yin, X. Yang, Y. Xu, and R. Lupoi, Solid-State Additive Manufacturing and Repairing by Cold Spraying: A Review, *J. Mater. Sci. Technol.*, 2018, **34**, p 440-457. <https://doi.org/10.1016/j.jmst.2017.09.015>
5. S. Pathak and G.C. Saha, Sustainable Development of Cold Spray Coatings and 3D Additive Manufacturing Components for Repair/ Manufacturing Applications: A Critical Review, *Coatings*, 2017, **7**, p 122-149. <https://doi.org/10.3390/coatings7080122>
6. S. Bagherifard and M. Guagliano, Fatigue Performance of Cold Spray Deposits: Coating, Repair and Additive Manufacturing Cases, *Int. J. Fatigue*, 2020, **139**, p 105744. <https://doi.org/10.1016/j.ijfatigue.2020.105744>
7. F.-L. Zavalan and A. Rona, A Workflow for Designing Contoured Axisymmetric Nozzles for Enhancing Additively Manufactured Cold Spray Deposits, *Addit. Manuf.*, 2023, **62**, p 103379. <https://doi.org/10.1016/j.addma.2022.103379>
8. X. Wang, B. Zhang, J. Lv et al., Investigation on the Clogging

- Behavior and Additional Wall Cooling for the Axial-Injection Cold Spray Nozzle, *J. Therm. Spray Tech.*, 2015, **24**, p 696-701. <https://doi.org/10.1007/s11666-015-0227-1>
9. O.C. Ozdemir and C.A. Widener, Influence of Powder Injection Parameters in High-Pressure Cold Spray, *J. Therm. Spray Tech.*, 2017, **26**, p 1411-1422. <https://doi.org/10.1007/s11666-017-0606-x>
  10. H. Assadi, F. Gärtner, T. Stoltenhoff, and H. Kreye, Bonding Mechanism in Cold Gas Spraying, *Acta Mater.*, 2003, **51**(15), p 4379-4394. [https://doi.org/10.1016/S1359-6454\(03\)00274-X](https://doi.org/10.1016/S1359-6454(03)00274-X)
  11. T. Schmidt, F. Gärtner, H. Assadi, and H. Kreye, Development of a Generalized Parameter Window for Cold Spray Deposition, *Acta Mater.*, 2006, **54**(3), p 729-742. <https://doi.org/10.1016/j.actamat.2005.10.005>
  12. V.K. Champagne, A. Nardi, D. Helfritsch, and M. Siopis, Material Properties, *Practical Cold Spray*. V.K. Champagne Jr., O.C. Ozdemir, A. Nardi Ed., Springer, Cham, 2021. [https://doi.org/10.1007/978-3-030-70056-0\\_5](https://doi.org/10.1007/978-3-030-70056-0_5)
  13. E. Irissou, D. Poirier, P. Vo et al., How to Unleash the Remarkable Potential of Cold Spray: A Perspective, *J. Therm. Spray Tech.*, 2022, **31**, p 908-919. <https://doi.org/10.1007/s11666-022-01363-7>
  14. D. Poirier, J.-G. Legoux, P. Vo, B. Blais, J.D. Giallonardo, and P.G. Keech, Powder Development and Qualification for High-Performance Cold Spray Copper Coatings on Steel Substrates, *J. Therm. Spray Technol.*, 2019, **28**, p 444-459.
  15. M. Siopis, A. Nardi, A. Espinal, L. Biniek, and T. Landry, Study of Nozzle Clogging During Cold Spray. [United Technologies Research Center]. Accessed 15 April 2020
  16. A. Sova, S. Grigoriev, A. Okunkova, and I. Smurov, Cold Spray Deposition of 316L Stainless Steel Coatings on Aluminium Surface with Following Laser Posttreatment, *Surf. Coat. Technol.*, 2013, **235**, p 283-289. <https://doi.org/10.1016/j.surfcoat.2013.07.052>
  17. K.C. Victor, H. Dennis, and P.F. Leyman (eds.). Magnesium Repair by Cold Spray (Aberdeen Proving Ground, MD, 2007), NASFSUR/FIN Proceedings. U.S. Army Research Laboratory
  18. W. Wong, E. Irissou, P. Vo et al., Cold Spray Forming of Inconel 718, *J. Therm. Spray Tech.*, 2013, **22**, p 413-421. <https://doi.org/10.1007/s11666-012-9827-1>
  19. W.Y. Li, S. Yin, X. Guo et al., An Investigation on Temperature Distribution Within the Substrate and Nozzle Wall in Cold Spraying by Numerical and Experimental Methods, *J. Therm. Spray Tech.*, 2012, **21**, p 41-48. <https://doi.org/10.1007/s11666-011-9685-2>
  20. O.C. Ozdemir and C.A. Widener, Gas Dynamics of Cold Spray & Control of Deposition. South Dakota School of Mines & Technology
  21. T. Suhonen, T. Varis, S. Dosta, M. Torrell, and J.M. Guilemany, Residual Stress Development in Cold Sprayed Al Cu and Ti Coatings, *Acta Mater.*, 2013, **61**(17), p 6329-6337. <https://doi.org/10.1016/j.actamat.2013.06.033>
  22. H. Koivuluoto and P. Vuoristo, Effect of Ceramic Particles on Properties of Cold-Sprayed Ni<sub>20</sub>Cr<sup>+</sup>Al<sub>2</sub>O<sub>3</sub> Coatings, *J. Therm. Spray Tech.*, 2009, **18**, p 555-562. <https://doi.org/10.1007/s11666-009-9345-y>
  23. H.B. Jung, J.I. Park, S.H. Park et al., Effect of the Expansion Ratio and Length Ratio on a Gas-Particle Flow in a Converging-Diverging Cold Spray Nozzle, *Met. Mater. Int.*, 2009, **15**, p 967-970. <https://doi.org/10.1007/s12540-009-0967-x>
  24. R.N. Raoelison, Y. Xie, T. Sapanathan, M.P. Planche, R. Kromer, S. Costil, and C. Langlade, Cold Gas Dynamic Spray Technology: A Comprehensive Review of Processing Conditions for Various Technological Developments Till to Date, *Addit. Manuf.*, 2018, **19**, p 134-159.
  25. L. Alonso, M.A. Garrido, and P. Poza, An Optimisation Method for the Cold-Spray Process: On The Nozzle Geometry, *Mater. Des.*, 2022, **214**, p 110387. <https://doi.org/10.1016/j.matdes.2022.110387>
  26. S.V. Klinkov, V.F. Kosarev, and V.N. Zaikovskii, Preliminary Study of Cold Spraying Using Radial Supersonic Nozzle, *Surf. Eng.*, 2016, **32**(9), p 701-706. <https://doi.org/10.1179/1743294415Y.0000000070>
  27. S.P. Kiselev, V.P. Kiselev, S.V. Klinkov, V.F. Kosarev, and V.N. Zaikovskii, Study of the Gas-Particle Radial Supersonic Jet in the Cold Spraying, *Surf. Coat. Technol.*, 2017, **313**, p 24-30. <https://doi.org/10.1016/j.surfcoat.2017.01.046>
  28. O.C. Ozdemir et al., Advancements in Cold Spray, *Practical Cold Spray*. V.K. Champagne Jr., O.C. Ozdemir, A. Nardi Ed., Springer, Cham, 2021. [https://doi.org/10.1007/978-3-030-70056-0\\_9](https://doi.org/10.1007/978-3-030-70056-0_9)
  29. K. Kowalski, P. Błasiak, and S. Pietrowicz, A Novel Cold Spray Process Flow Technique: A Numerical Investigation, *Int. J. Heat Mass Transf.*, 2024, **218**, p 124817. <https://doi.org/10.1016/j.ijheatmasstransfer.2023.124817>
  30. R.N. Raoelison, S. Msolli, S. Deng, A. Vashishtha, A. Sharma, D. Callaghan, and R.A. Raghavendra, Concept of Aerospike Nozzle for Cold Spray Additive Manufacturing—Towards a Potential Solution for Preventing the Issue of Clogging, in Proceedings of the ITSC 2023. *Thermal Spray 2023: Proceedings from the International Thermal Spray Conference*. Québec City, Canada. (pp. 229-234). ASM. <https://doi.org/10.31399/asm.cp.itsc2023p0229> (2023)
  31. H. Sharma, A. Vashishtha, P. Lovaraju, and E. Rathakrishnan. Characteristics of sonic and supersonic co-flow jets, in Proceedings of 2nd International Conference on Recent Advances in Experimental Fluid Mechanics (RAEFM) (2008)
  32. H. Sharma, A. Vashishtha, E. Rathakrishnan, and P. Lovaraju, Experimental Study of Overexpanded Co-Flowing Jets, *Aeronaut. J.*, 2008, **112**(1135), p 537-546. <https://doi.org/10.1017/S0001924000002499>
  33. A.K. Sharma, A. Vashishtha, D. Callaghan, C. Nolan, S. Bakshi, M. Kamaraj, and R. Raghavendra, Particle Acceleration Through Coaxial Co-Flow Nozzles for Cold Spray Applications, in Proceedings of the ITSC2022. *Thermal Spray 2022: Proceedings from the International Thermal Spray Conference*. Vienna, Austria. (pp. 676-682). ASM. <https://doi.org/10.31399/asm.cp.itsc2022p0676> (2022)
  34. A.K. Sharma, A. Vashishtha, D. Callaghan, S.R. Bakshi, M. Kamaraj, and R. Raghavendra, Investigation of a Modified Circular Nozzle for Cold Spray Applications, in Proceedings of the ITSC 2023. *Thermal Spray 2023: Proceedings from the International Thermal Spray Conference*. Québec City, Canada. (pp. 235-241). ASM. <https://doi.org/10.31399/asm.cp.itsc2023p0235> (2023)
  35. Noise from Imperfectly Expanded Supersonic Coaxial Jets, Marco Debiassi and Dimitri Papamoschou, *AIAA J.*, 2001, **39**(3), p 388-395. <https://doi.org/10.2514/2.1348>
  36. M. Meyer and R. Lupoi, An Analysis of the Particulate Flow in cold Spray Nozzles, *Mech. Sci.*, 2015, **6**(2), p 127-136.
  37. X. Suo, S. Yin, M.P. Planche, T. Liu, and H. Liao, Strong Effect of Carrier Gas Species on Particle Velocity During Cold Spray Processes, *Surf. Coat. Technol.*, 2015, **268**, p 90-93. <https://doi.org/10.1016/j.surfcoat.2014.04.039>
  38. ANSYS, Inc, ANSYS Fluent User's Guide, R2 Release (2021)

39. A “Private Communication”, with Department of Metallurgical and Material Engineering, Indian Institute of Technology Madras, India
40. O.Ç. Özdemir, 5—Process parameters and control, Editor(s): Victor K. Champagne, Dennis Helfrich, Mostafa Hassani Gangaraj, *Advances in Cold Spray (Second Edition)*, (Woodhead Publishing, 2023), pp. 89-134. <https://doi.org/10.1016/B978-0-08-103015-8.00005-0>
41. J.D. Anderson, *Modern Compressible Flow: With Historical Perspective*, McGraw-Hill, United Kingdom, 2004.
42. D. Guo, M. Kazasidis, A. Hawkins et al., Cold Spray: Over 30 Years of Development Toward a Hot Future, *J. Therm. Spray Tech.*, 2022, **31**, p 866-907. <https://doi.org/10.1007/s11666-022-01366-4>
43. Q. Wu, J. Su, W. Zhao, J. Li, K. Zhang, and L. Wang, Determination of Critical Velocity of Cold-Sprayed NiCoCrAlY Coating via Arbitrary Lagrangian-Eulerian (ALE) Method of Finite Element Simulation, *Coatings*, 1992, **2023**, p 13. <https://doi.org/10.3390/coatings13121992>
44. T. Hussain, Cold Spraying of Titanium: A Review of Bonding Mechanisms, Microstructure and Properties, *Key Eng. Mater.*, 2012, **533**, p 53-90.
45. T.J. Eden, O.C. Ozdemir, and V.K. Champagne, Process Description, *Practical Cold Spray*. V.K. Champagne Jr., O.C. Ozdemir, A. Nardi Ed., Springer, Cham, 2021. [https://doi.org/10.1007/978-3-030-70056-0\\_2](https://doi.org/10.1007/978-3-030-70056-0_2)
46. S. Rajkumar, P. Vasanthakumar, A.K.S. Moorthi, and E. Rathakrishnan, Supersonic Jet Mixing in the Presence of Two Annular Co-Flow Streams, *Int. J. Turbo Jet-Eng.*, 2024, **41**(1), p 103-110. <https://doi.org/10.1515/tjj-2022-0048>

**Publisher’s Note** Springer Nature remains neutral with regard to jurisdictional claims in published maps and institutional affiliations.